Nano Energy 26 (2016) 533–540

Contents lists available at ScienceDirect

Nano Energy

journal homepage: www.elsevier.com/locate/nanoen

Morphology-dependent performance of nanostructured Ni_3S_2/Ni anode electrodes for high performance sodium ion batteries

Xiaosheng Song [a,b,c], Xifei Li [b,c,*], Zhimin Bai [a,*], Bo Yan [a,b,c], Dejun Li [b,c], Xueliang Sun [b,c,d,*]

[a] Beijing Key Laboratory of Materials Utilization of Nonmetallic Minerals and Solid Wastes, National Laboratory of Mineral Materials, School of Materials Science and Technology, China University of Geosciences, Beijing 100083, China
[b] Energy & Materials Engineering Centre, College of Physics and Materials Science, Tianjin Normal University, Tianjin 300387, China
[c] Tianjin International Joint Research Centre of Surface Technology for Energy Storage Materials, Tianjin 300387, China
[d] Nanomaterials and Energy Lab, Department of Mechanical and Materials Engineering, University of Western Ontario, London, Ontario, Canada N6A 5B9

ARTICLE INFO

Article history:
Received 11 April 2016
Received in revised form
1 June 2016
Accepted 11 June 2016
Available online 14 June 2016

Keywords:
Morphology evolution
Nickel foam
Nickel sulfide
Sodium ion batteries

ABSTRACT

Transition metal sulfides have been treated as promising materials for lithium-ion battery, and recently more and more attention has been paid to its applications in sodium-ion batteries. In our context, three Ni_3S_2 nanostructures directly grown on Ni foam were successfully designed using a facile hydrothermal method. The influences of the morphology on the performance evolution for sodium-ion batteries were studied in detail. As a result, it was found that the initial drop, gradual increase, convex type decline and concave type decline in the performance evolutions were mainly controlled by R_{ct}, R_{sf}, pulverization, and internal stress, respectively. More importantly, our results indicated that the clustered network-like structure was beneficial for the cycling and rate performance, while the rod-like structure was suitable for the cyclic stability of these electrodes.

1. Introduction

Limited lithium resources possibly prevent the future development of lithium-ion batteries (LIBs), for instance, the recent price of Li_2CO_3 frequently increases, being an obvious obstacle of advanced LIB application. Precisely for this reason, room-temperature sodium-ion technology has staged a comeback, particularly for large-scale stationary energy storage applications. The similar chemical properties in some aspects exist between sodium and lithium, as a result, the investigations on anode [1–3] and cathode [4–6] materials of the sodium-ion batteries (SIBs) were mainly "borrowed" from LIBs. For example, as an anode material of LIBs, SnO_2 has been successfully studied for SIB anodes [7–10]. So far, most of anode materials in SIBs are impeded by either low specific capacity or large volume expansion. Therefore, it is necessary to develop high performance anode materials for SIBs.

Some transition metal chalcogenides have been successfully employed as anodes for LIBs [11,12], based on a conversion reaction mechanism. The multiple electron involved conversion reaction leads to high theoretical specific capacity of transition metal chalcogenides [2]. Take into account the high electrochemical activity of nickel ion and strong reducibility of sulfur ion, nickel sulfides have been investigated as attractive anode electrode materials in LIBs [13–15]. Nickel sulfide can occur in various phases and compositions, such as NiS, NiS_2, Ni_3S_2, Ni_3S_4, Ni_7S_6, Ni_9S_8, and so on [16]. Among them, the researchers focused many attentions on Ni_3S_2 due to its lower room temperature resistivity of approximately $1.2 \times 10^{-4}\ \Omega \cdot cm$ [17], thus, it is expected that Ni_3S_2 anode may exhibit enhanced performance for SIBs. However, on one hand, few reports focused on Ni_3S_2 for SIB anodes as a result of larger volume expansion and worse electrode conductivity. On the other hand, traditional casting-derived Ni_3S_2 electrodes were hindered by the poor interfacial electrical contact between active materials and current collectors [18–20]. One of the effective methods to improve the conductivity of Ni_3S_2 electrodes is to design Ni_3S_2 directly grown on the current collector, such as nickel foam, to avoid the additive of polymer binder with poor electrical conductivity [21]. For example, the nanostructured Ni_3S_2 films were deposited on Ni foam via a hydrothermal route, showing high reversible capacity of 421 mA h g^{-1} after 60 cycles at a current density of 50 mA g^{-1} for LIBs [22]. The design of Ni_3S_2–PEDOT on Ni foam substrate showed stable cycling performance with a capacity of 280 mA h g^{-1} after 30 cycles between 0.5 and 2 V for SIBs [23]. In addition, the 3D porous structure of Ni foam can facilitate the penetration of electrolyte, shorten the ion diffusion distance, and further

* Corresponding authors at: Energy & Materials Engineering Centre, College of Physics and Materials Science, Tianjin Normal University, Tianjin 300387, China (X. Li). Tel.: +86 22 23766526; fax: +86 22 23766503.
E-mail addresses: xfli2011@hotmail.com (X. Li), zhimibai@cugb.edu.cn (Z. Bai), xsun@eng.uwo.ca (X. Sun).

http://dx.doi.org/10.1016/j.nanoen.2016.06.019
2211-2855/

enhance the transport kinetics [24]. On the basis of previously published literature [23,25,26], the anode performance of Ni_3S_2 is still not satisfied for SIBs. Therefore, how to enhance the anode performance of Ni_3S_2 has been challenging for SIBs.

In our present investigation, we have studied the morphology-dependent performance evolutions of Ni_3S_2 directly grown on nickel foam (Ni_3S_2/Ni) as the anode materials for SIBs. It is expected that the use of electrode materials with different designed morphologies will have a bright prospect to improve the performance of batteries. For example, size-dependent sodium storage properties of $Na_2C_6O_6$ -based organic electrodes have been studied [27]. It was demonstrated that rational morphological control can lead to significantly improved sodium storage performance. P2-$Na_xCo_yMn_{1-y}O_2$ (y=0, 0.1) with hexagonal flakes and hollow spheres morphologies have been compared [28], with a result of enhanced cycling performance of the spherical over the flake-like morphology which is attributed to smaller volume changes of the unit cell of the spheres during cycling. Few reports were studied, however, to focus on the relationship between morphologies and electrochemical performances of Ni_3S_2 anode material for SIBs. It is believed that different morphologies and structures provide different electrochemical reaction interfaces, even some special chemical environments involved with quantum size effect, thus, the influence of morphologies on electrochemical properties is necessary to be clarified.

2. Experimental

2.1. Growth of Ni_3S_2 on Ni foam

Several nanostructured Ni_3S_2 compounds were synthesized by the *in situ* growth on Ni foam via a simple hydrothermal method. Briefly, Ni foams punched in the form of 10 mm disks in diameter were sonicated in the ethanol and the oxalic acid orderly to remove the oily impurity and the surface oxide layer. After rinsing and drying, the cleaned Ni foam pieces were transferred into Teflon stainless steel autoclave with $Na_2S_2O_3$ solution (30 ml, 0.04 M). The samples were generated at 100 °C (marked as NS-I), 120 °C (NS-II), and 150 °C (NS-III) for 4 h in the sealed autoclave. At 90 °C in our system, it was found the Ni foam was not sulfurated well as shown in Fig. S1a. With precisely weight by a microbalance (0.1 μg, VMT5, Mettler Toledo), the weight differences (Δ_m) of Ni foam before and after sulfuration were received. So according to the reaction ($3Ni + 2S = Ni_3S_2$), the weight of Ni_3S_2 ($M_{Ni_3S_2}$) can be derived from $M_{Ni_3S_2} = \Delta_m \times 240.1/64$ [29].

2.2. Characterization

X-ray powder diffraction (XRD) patterns were collected on a Bruker AXS D8 advance X-ray diffractometer with Cu Kα radiation (λ=0.154056 nm) at the 2θ range of 10–80°. The morphologies of the samples were observed using Hitachi-SU8010 type field emission scanning electron microscope (FE-SEM), and the observation of the samples after electrochemical cycles was performed on the same apparatus with the assistance of its supporting vacuum transfer box. Transmission electron microscopy (TEM, JEOL JEM-3000F) and X-ray photoelectron spectroscopy (XPS, VG ESCALAB MK II) were employed to verify the nanostructure and the surface chemical composition of the samples.

2.3. Electrochemical behavior with sodium

Without any polymer binder and conductive additive, the synthesized Ni_3S_2/Ni nanostructures were directly employed as working electrode. Besides the Ni_3S_2/Ni working electrodes, sodium pieces used as the counter electrode, microporous polypropylene film as the separator, and 1 M $NaClO_4$ dissolved in EC: DMC (1:1 in volume) with 5% FEC as electrolyte were encapsulated in CR2032-type coin cells. The assembly process was operated in a high purity argon-filled dry glove box. The cells were galvanostatically discharged and charged in the range of 0.01–3 V (*vs.* Na/Na^+) using a Land CT2001 battery tester. At a fixed voltage range, cyclic voltammogram (CV) of the samples was measured at a scan rate of 0.1 mV s^{-1} using Princeton Applied Research VersaSTAT 4 electrochemical workstation. On the same workstation, electrochemical impedance spectroscopy (EIS) measurements of the samples were systematically performed at an amplitude of 5 mV over the frequency range from 100 KHz to 0.01 Hz.

3. Results and discussion

3.1. Characterization of the Ni_3S_2/Ni nanostructures

The SEM analysis and the XRD patterns of the Ni_3S_2/Ni nanostructures were examined to study the morphology and composition. During the hydrothermal reaction, supersaturation, which is considered as an important parameter for the kinetics of crystallization, is susceptible to the reaction temperature. However, in the study of Co_9S_8/RGO/Ni_3S_2 on Ni foam, Zhang et al. found that the temperature only affects the nanoflakes' size and depth [30]. For $Co(CO_3)_{0.35}Cl_{0.20}(OH)_{1.10}$ nanoneedle arrays on Ni foam, it has been discovered that their SEM images showed similar features when synthesis temperature was changed from 95 °C to 105 °C and 115 °C [31]. Conversely, a significant influence of temperature on the morphologies was found in our investigation. As shown in Fig. 1a, porous net-structured nanosheets of NS-I with rough surfaces were generated at 100 °C. When the synthesis temperature increased to 120 °C, the morphology of NS-II changed into a “clustered network”-like nanostructure with opening channels, which seemingly had a trend to form bars. At higher temperature (150 °C), a rod-like nanostructure with nanometers from tens to hundreds can be observed in Fig. 1c. Thus, it can be concluded that at lower temperature, the morphology prefers to sheet-like structure, and as the temperature rises, the sheet-like structure will gradually turn to a rod-like structure. The insets represent corresponding low-magnification SEM images, confirming uniform distribution of Ni_3S_2 on Ni foam. It is worth noting that these different morphologies and size dimensions of Ni_3S_2/Ni electrodes will result in different dynamic processes of sodium storage, and then affect the electrochemical performance.

The XRD patterns of NS-I, NS-II, and NS-III are shown in Fig. 1d. In addition of three peaks at 2θ=44.5°, 51.9°, and 76.4° originating from Ni foam (JCPDS no. 87-0712), the rest peaks are in well accordance with Ni_3S_2 of heazlewoodite phase (JCPDS no. 86-1802), which confirms the successful design of Ni_3S_2/Ni nanostructures. To further verify the purity, the XRD patterns of the samples synthesized at 90 °C and 180 °C, as well as at 120 °C with different concentrations of $Na_2S_2O_3$ were examined in Fig. S1. It can be seen in Fig. S1a that at high temperature (180 °C), the product became a mixture of Ni_3S_2 and a new phase of NiS (JCPDS no. 12-0041). As the concentration of $Na_2S_2O_3$ increased, more impure peaks emerged (Fig. S1b). For example, in the case of 0.1 M, the extra peak at near 18.4° can be assigned to NiS. As a result, it can be deduced that the optimized synthesis parameter results in the formation of Ni_3S_2 with high purity following the reaction as below:

$$3Ni + 2Na_2S_2O_3 \rightarrow Ni_3S_2 + 2Na_2SO_3$$

TEM and XPS of NS-II were carried out to identify the nanostructure and elementary composition, as shown in Fig. 2. The clustered network-like structure is clearly observed in Fig. 2a, which is consistent with the SEM image in Fig. 1b. Fig. 2b shows

the high-resolution transmission electron microscopy (HR-TEM) image, and its insets represent the fast Fourier transform (FFT) and the inverse fast Fourier transform (IFFT) images. The FFT image shows a polycrystalline feature of Ni_3S_2 and the measured lattice fringe in IFFT image with an interplane spacing of 0.28 nm corresponds to the (110) plane of Ni_3S_2. Corrected with C 1 *s*

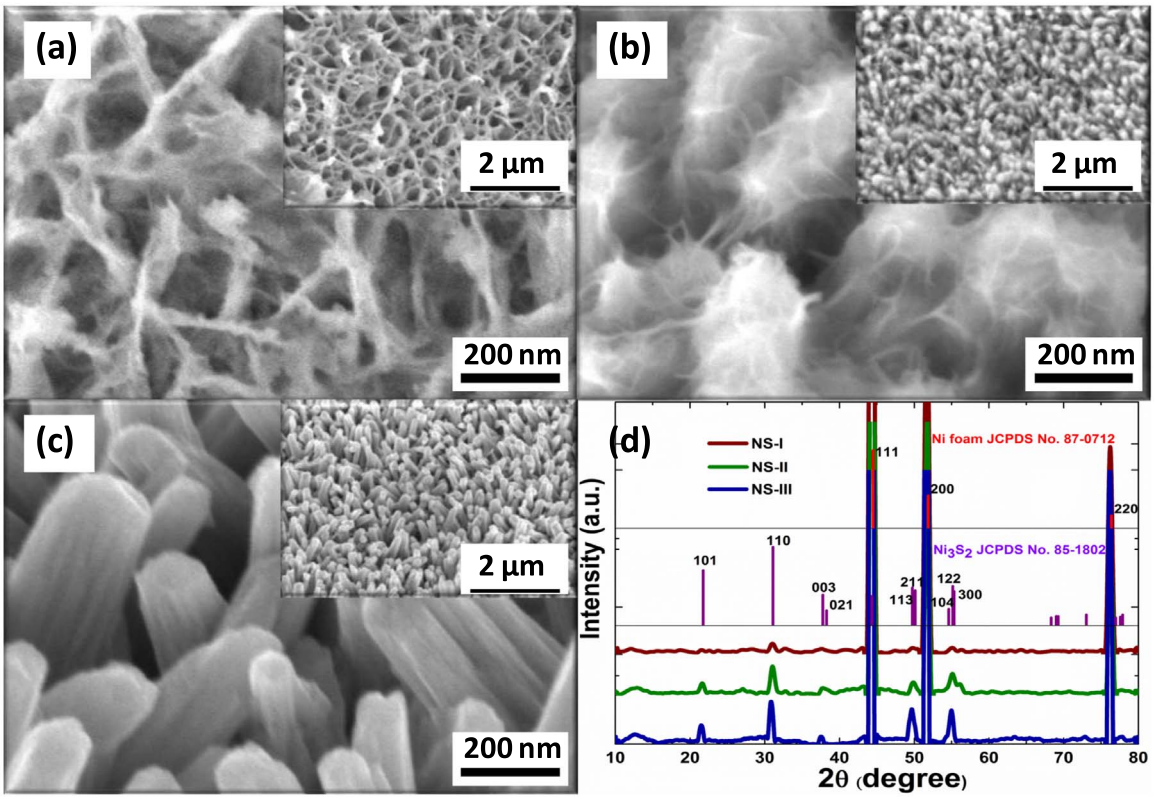

Fig. 1. High- and low-magnification (the insets) SEM images of (a) NS-I, (b) NS-II, and (c) NS-III. (d) XRD patterns of these Ni_3S_2/Ni composites.

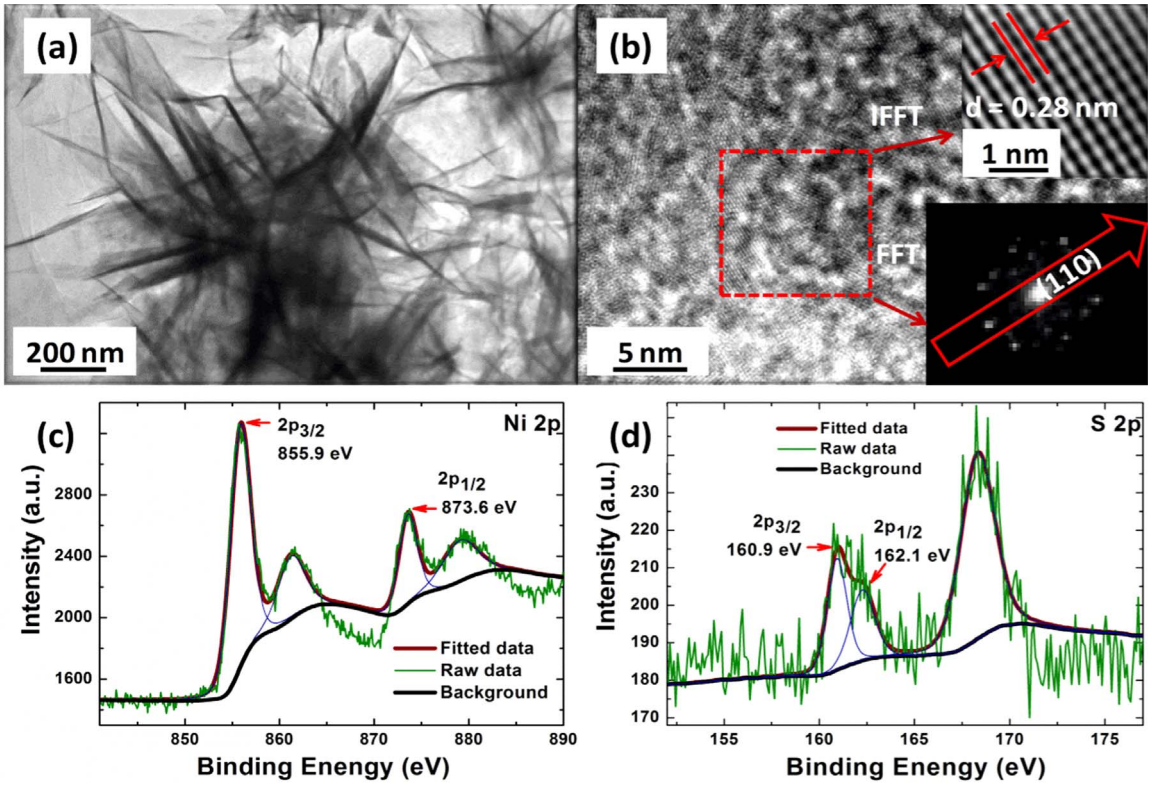

Fig. 2. (a) TEM and (b) high resolution TEM of NS-II. The insets in (b): fast Fourier transform (FFT) and the inverse fast Fourier transform (IFFT) images. (c) Ni 2p and (d) S 2p XPS spectra of this sample.

(284.6 eV) as the reference, Ni 2*p* and S 2*p* XPS peak-fitting results of NS-II are shown in Fig. 2c and d. In the Ni 2*p* XPS spectrum, two main peaks at 873.6 eV and 855.9 eV can be assigned to Ni $2p_{1/2}$ and Ni $2p_{3/2}$, respectively. The other two peaks correspond to the accompanied satellite peaks of Ni $2p_{1/2}$ and Ni $2p_{3/2}$. In S 2*p* region, the peaks at 162.1 eV and 160.9 eV originate from S $2p_{1/2}$ and S $2p_{3/2}$, respectively, and they respond to the S^{2-}. The peak at around 168.3 eV might be due to the residual $S_2O_3^{2-}$ on the surface of Ni_3S_2/Ni[32–34]. Considering in conjunction with XRD patterns, the influences of $S_2O_3^{2-}$ on electrochemical performance may be neglectable. In general, the peaks in Ni 2*p* and S 2*p* spectra show obvious characteristics of Ni_3S_2 [15,35–37], which are in agreement with the XRD and HR-TEM results.

3.2. Electrochemical performance of the Ni_3S_2/Ni nanostructures

The charge/discharge profiles and CV curves could effectively elucidate the oxidation/reduction of sodium storage process. The charge/discharge profiles of NS-I, NS-II, and NS-III at a current rate of 50 mA g^{-1} at the potential range of 0.01–3 V (*vs.* Na/Na^+) are shown in Fig. 3a–c, respectively. The corresponding CV curves are compared in Fig. 3d–f. From an overall perspective, both charge/discharge profiles and CV curves of these three electrodes show similar characteristics. The voltage plateaus near 0.6 V in the first discharge process could be attributed to the conversion reaction in which Ni_3S_2 converts into Ni particles embedded in Na_2S matrixes, accompanied by the formation of SEI. In subsequent discharge process, the formation of ultrafine nanoclusters (see Fig. 6) results in improved kinetics, and hence pushes the plateaus to near 1.0 V. These are proved by the reduction peaks at 0.6 V in the first CV scan and the reduction peaks at about 1.0 V in the following CV scans. Besides, in the charge process, the voltage plateaus at near 1.6 V and the sloping segments in the range of 1.1–1.5 V agreed by oxidation peaks at 1.6 V and 1.4 V in CV scans could be attributed to the oxidation of Ni to Ni_3S_2 and the decomposition of SEI [38]. It is worth mentioning that both discharge and charge specific capacities of these three electrodes tend to a down and up trend, as shown in the insets in Fig. 3a–c, supported by the CV curves in Fig. 3d–f. On the other hand, there are some differences in the charge/discharge profiles and CV curves among these three electrodes. In the 2nd and 3rd CV scans of NS-I and NS-III, besides the main reduction peak at around 1.0 V, there is an extra reduction peak at near 0.8 V, but for NS-II, there is only a single reduction peak. Both the extra peak of NS-I and NS-III and the single peak of NS-II shift to right slightly and the peak shift feature vanished after 5 cycles.

The cycling performance and rate performance of NS-I, NS-II, and NS-III are compared in Fig. 4 and Fig. S2. The NS-II shows an initial discharged capacity of 373.4 mA h g^{-1}, and it still delivers a specific capacity of 315.3 mA h g^{-1} after 100 cycles, resulting in a high capacity retention ratio of 90.6% (calculated with the first reversible capacity of 348.2 mA h g^{-1}). In comparison with NS-II, NS-I reveals a higher initial specific capacity of 404.4 mA h g^{-1}, which may be caused by its more opened structure, but a lower capacity retention ratio of 62.2% is obtained after 100 cycles. Despite the better cycling stability of NS-III than NS-II, it presents much lower specific capacity. More importantly, it can be seen in Fig. 4b that NS-II exhibits better rate performance than NS-I and NS-III. Additional, one can see that the cyclic profile consists of several typical regions. For instance, the NS-II profile can be divided into four regions: the initial drop of the 1–5th cycles as region-I, the gradual rise of the 5–55th cycles as region-II, the convex type decline of the 55–99th cycles as region-III, and the concave type decline shown in Fig. S2 after 99 cycles as region-IV. The curves of NS-I and NS-III reveal similar trend.

It is worth mentioning that the performance of these three samples follows a possible trend with their morphologies related. The higher capacity of NS-I benefits from its porous net-structured

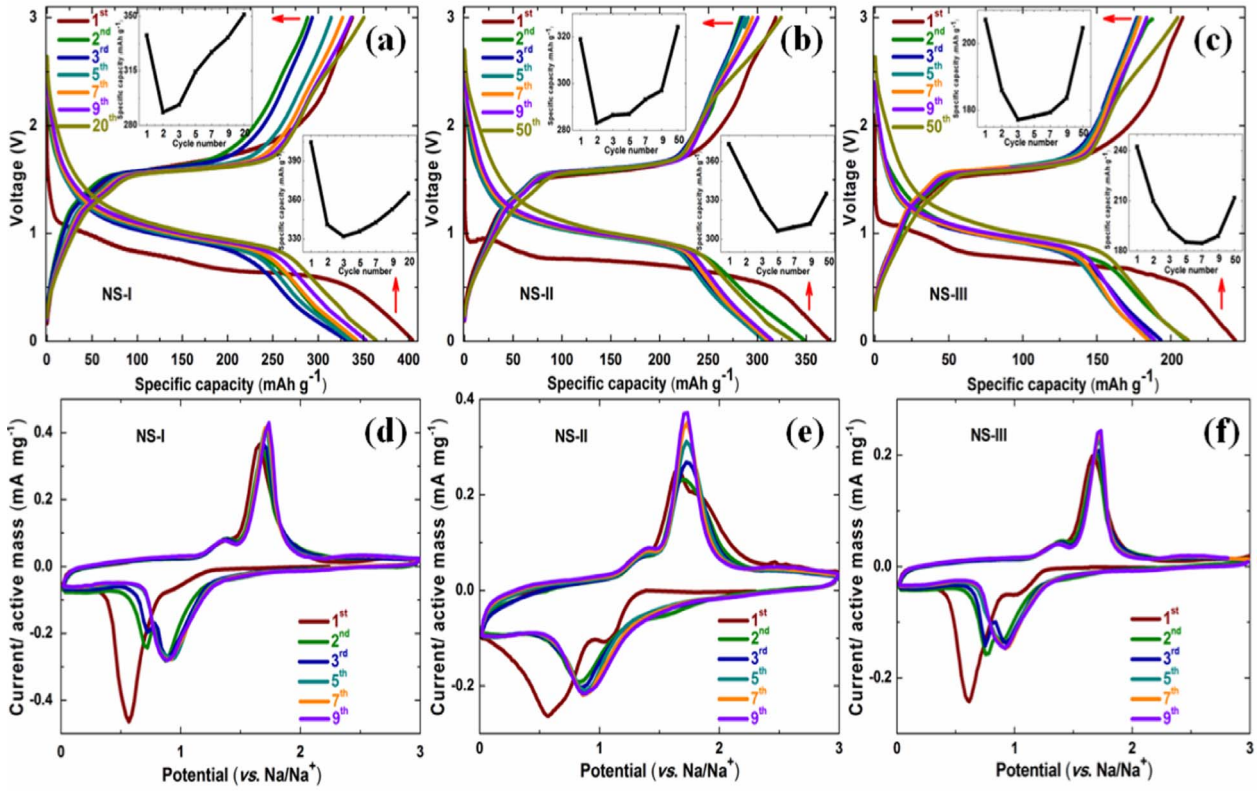

Fig. 3. (a, b, and c) Charge/discharge profiles and (d, e, and f) CV curves at selected cycles of NS-I, NS-II, and NS-III. The insets in (a, b, and c) represent the specific capacities as a function of the selected cycles.

nanosheets, but this morphology is more deformed during cycling, leading to low capacity retention. Similarly, the rod-like structure is available to deliver better cycling stability, but larger and thicker particle results in much lower specific capacity. Thus, the better cycling and rate performance of NS-II can be ascribed to its porous clustered network-like structure. The porous network structure is available to improve the utilization coefficient of active material, and the clustered structure prevents the complete obliteration of the original morphology. As a result, the porous clustered network-like structure of NS-II provides a more effective and more stable pathway for Na^+ ion transfer, resulting in higher capacity than NS-III, and better cycling stability than NS-I. To further highlight the enhanced SIB performance of the clustered network-like NS-II, Table S1 compares the discharge capacities of NS-II and previously reported nickel sulfide based electrodes for SIBs. Obviously, our clustered network-like Ni_3S_2/Ni reveals much better capacity retention than those of Ni_3S_2/Ni microparticles [23], Ni_3S_2@MoS_2 nanofiber [39], NiS_2 powder [40], and Ni_xS_6/Ni_3S_2/Ni_7S_6 packed layer [41].

EIS measurements have been systematically performed to explain region-I and region-II. In our architectures, opening channels among the nanostructures can be used as the electrolyte reservoirs, making each particle exposed to the electrolyte from several facets. Thus, the reaction between Na and Ni_3S_2 occurs simultaneously in parallel to each particle, from the envelope toward the center of the particle. Such a structure is extremely similar to the ultrathin transition metal oxide electrodes reported by Aurbach and coworkers [42].

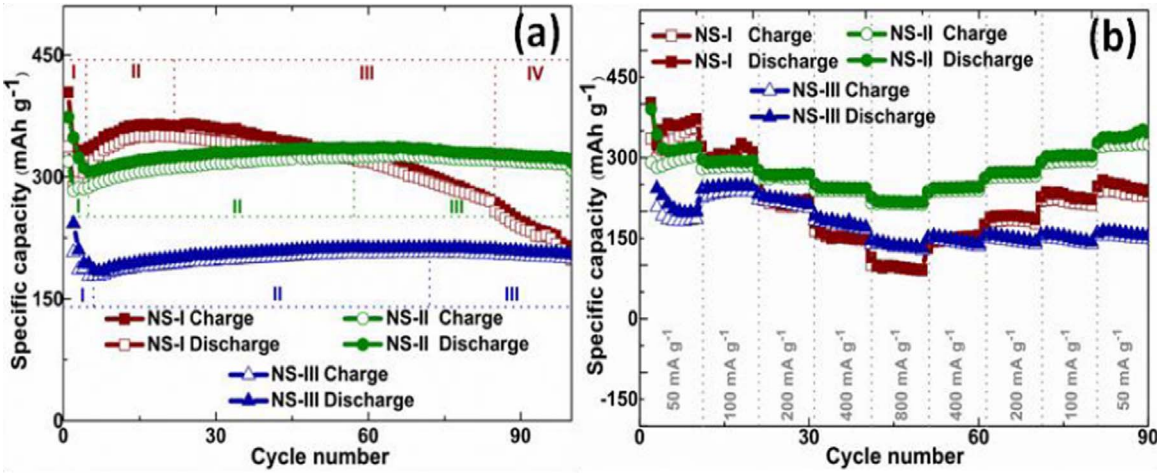

Fig. 4. (a) Cycling performance at the current density of 50 mA h g^{-1} and (b) rate capability of NS-I, NS-II, and NS-III.

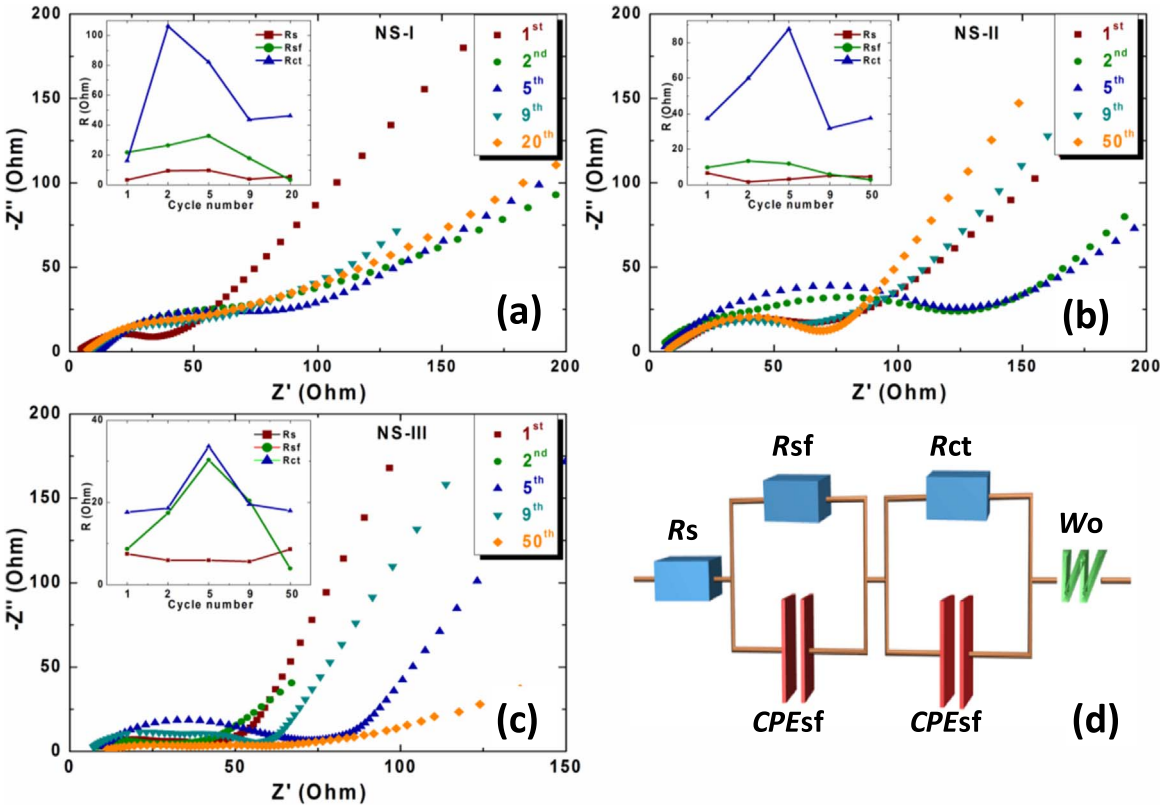

Fig. 5. Nyquist plots of (a) NS-I, (b) NS-II, and (c) NS-III after selected cycles at discharged state. The insets: corresponding values of R_s, R_{sf}, and R_{ct} with varied cycle numbers. (d) equivalent circuit used to simulate the resultant Nyquist plots.

Therefore, the Nyquist plots were fitted using a remarkably analogical equivalent circuit exhibited in Fig. 5d, which composes of an ohmic resistance (R_s), two *RC* parallel elements in series describing the SEI (R_{sf} and CPE_{sf}) and charge transfer (R_{ct} and CPE_{ct}), and Warburg impedance (W_o) for solid state diffusion of Na^+ ions [43]. In Fig. 5a–c, the semicircles at the high and middle frequency regions can be assigned to the R_{sf} and R_{ct}, and the oblique lines at the low frequency regions reflect the Warburg impedance. The values of R_s, R_{sf}, and R_{ct} of NS-I, NS-II, and NS-III were calculated using Zview2 software, and the results are shown in the insets in Fig. 5a–c. Of all the cases, during region-I and region-II, the values of R_s change little, indicating the little contribution of R_s to the performance evolutions. As for R_{ct} before the 5th cycle, there are significant increases; more interestingly, R_{ct} reduces to a relatively stable state after the 5th cycle. So the drops of the specific capacity in region-I are mainly caused by the increases of R_{ct}. Considering the decreases of R_{sf} after the 5th cycle, the gradually rises of the specific capacity in region-II can be attributed to the slow dissolution of the SEI accumulated in the first few cycles [44,45]. Specially, the increase feature of R_{sf} before the 5th cycle is applicable to NS-I and NS-III, but not to NS-II, which is in accordance with the CV curves. Therefore, the extra reduction peak at near 0.8 V in the 2nd and 3rd CV scans of NS-I and NS-III can be ascribed to the formation of new SEI.

3.3. Relationship between morphologies and performances

The SEM images of these three electrodes at discharged state after 1, 5, and 50(20) cycles were examined to study the influence of morphology which can be seen in Fig. 6. The low-magnification SEM images are shown in the insets. For NS-I and NS-III, more SEI may be created because of the generated ultrafine Ni particles' catalytic action located on the surfaces of the net-structured nanosheets and the rods, as shown in Fig. 6a and g. This can be verified by the initial rise of R_{sf} in the EIS measurements of NS-I and NS-III. More interestingly, the Ni particles of NS-II are mainly distributed in the gaps of the network-like structure in Fig. 6d, thus these nanoparticles may not directly affect the SEI, resulting in no extra reduction peak in the 2nd and 3rd CV scans in Fig. 3e. Furthermore, high free energy of the generated ultrafine Ni particles can provide extra energy to assist the activation of Ni_3S_2, corresponding to the slight peak shift in CV scans during the region-I. It should be noted that the high energy also causes the agglomeration of these Ni particles (see Fig. 6b, e, and h), leading to the prodigious increase of R_{ct}. When the size of the agglomerating particles exceeds the critical dimension, they will lose their quantum size effect. As a result, the extra peak and peak shift in CV measurement have disappeared from the 5th cycle in all cases.

On the other hand, during the region-II, the Ni particles tend to form a dispersed, disorder distribution to get a stable condition in Fig. 6c, f, and i. In the process of these transformations, however, they are controlled by the original morphologies. As shown in Fig. 6f, the bottoms of the agglomerated particles of NS-II after 50 cycles are strung together using the nets as the ropes, with the porous structure reserved. In Fig. 6i, the agglomerated particles of NS-III are confined to the rod-like structure, which is more close to the original appearance. It is worth mentioning that this strong sustainability results in the better cycling stability of NS-III as shown in Fig. S2. As for NS-I in Fig. 6c, the trace of the original morphology after 20 cycles has almost disappeared. Its agglomerations tend to fall from the "sheets" and the morphology change to a porous structure without order. It is believed that these more disorder particles prefer to spherical agglomeration with larger scale during the subsequent cycling processes. To verify it, the morphology of NS-I after 50 cycles has been shown in Fig. S3 which reveals much larger particles.

To illuminate the region-III and region-IV in Fig. 4a and Fig. S2, the SEM images of NS-II after 100 cycles and 150 cycles have been researched. As shown in Fig. S4a, the twisted upheavals reflect the agglomeration and pulverization, which result in the decrease of the specific capacity in region-III. The faster decay of the specific capacity

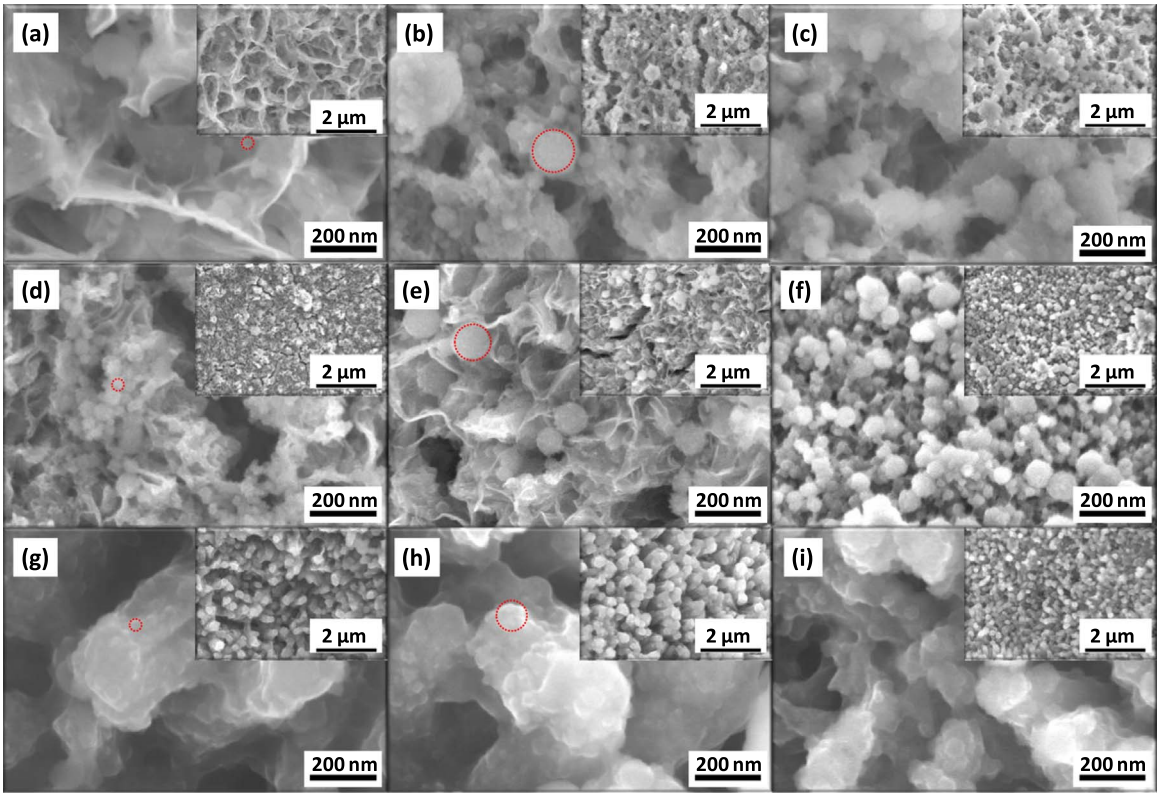

Fig. 6. Morphology evolutions of (a, b, and c) NS-I, (d, e, and f) NS-II, and (g, h, and i) NS-III after (a, d, and g) 1, (b, e, and h) 5, and (f and i) 50 cycles, (c) is after 20 cycles. Insets: corresponding low-magnification SEM images.

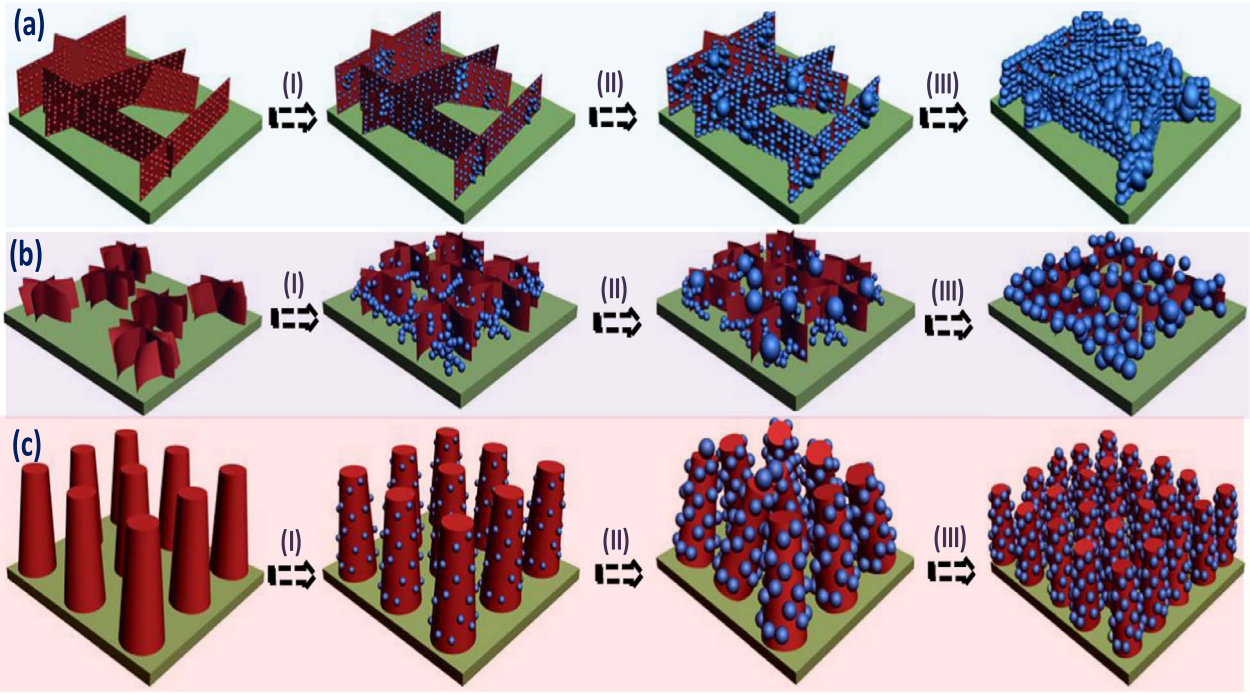

Scheme 1. Proposed mechanism for the morphology evolutions of (a) NS-I, (b) NS-II, and (c) NS-III. (I), (II), and (III) represent the transformations of NS-I, NS-II, and NS-III from 0 to 1–5 to 50 cycles. Specially, transformation (III) in Fig. a is to 20 cycle.

of NS-I than NS-II and NS-III is due to its larger spherical agglomeration. Additional, the marked sections in Fig. S4a show that the active materials tend to exfoliate from the substrate of Ni foam due to the internal stress. For the case after 150 cycles, a selected region where the exfoliation can be clearly observed is shown in Fig. S4b. From the convex type decline to the concave type decline, the major controlling factor has changed from agglomeration to internal stress.

To further illustrate the morphology variation during the electrochemical performance evolution, the schematic illustration of the morphology of NS-I, NS-II, and NS-III with varied cycle numbers is shown in Scheme 1. Typically, net-structured nanosheet of NS-I, clustered network-like nanostructure of NS-II, and rod-like nanostructure of NS-III have been successfully synthesized via a facile hydrothermal process. After 1 cycle, the ultrafine Ni nanoclusters are formed on the surfaces of NS-I and NS-III, but they exist in the gaps of NS-II. It is the reason why R_{sf} of NS-II is different from NS-I and NS-III. During a reunion and inflation process, Ni clusters turn to form much larger particles with the loss of catalytic activity at the 5th cycle. After 50 cycles, these electrodes of NS-II and NS-III are changed to a decentralized distribution in comparison to the original morphology. For NS-I, the appearance have almost been out of the control of the original morphology after 20 cycles, resulting in rapid capacity drop. In subsequent cycles, these electrodes undergo the similar process of gradual distortion, pulverization, and exfoliation. One can see that the anode morphologies change upon cycling. And the morphology evolution of the anode materials have a significant impact on the battery performance. As a result, there is a close connection between the morphology and the electrochemical performance. Therefore, the study of their relationship is meaningful for designing high performance electrode materials for SIBs.

4. Conclusion

Three Ni_3S_2/Ni nanostructured electrodes, NS-I, NS-II, and NS-III, with different morphologies have been synthesized by controlling the synthesis temperature at 100 °C, 120 °C, and 150 °C, respectively. Due to their high specific capacities and controllable morphologies, these designed electrodes show great potential for SIBs. The special performance evolutions have been investigated in details. It is found that R_{ct}, R_{sf}, pulverization, and internal stress are the major contributors for the initial drop, gradual increase, convex type decline and concave type decline of reversible capacity, respectively. On basis of the analysis of the relationship between morphology evolution and performance evolution, enhanced cycling and rate performance of NS-II benefit from the clustered network-like structure, and the rod-like structure of NS-III is beneficial to its cycling stability.

Acknowledgments

This research was supported by the National Natural Science Foundation of China (51572194), the Key Project of Tianjin Municipal Natural Science Foundation of China (14JCZDJC32200), Academic Innovation Funding of Tianjin Normal University (52XC1404), LPMT (Laboratory of Precision Manufacturing Technology), CAEP (China Academy of Engineering Physics) (KF14006), the program of Thousand Youth Talents in Tianjin of China, and XS thanks support from the Natural Science and Engineering Research Council of Canada and the Canada Research Chair Program.

Appendix A. Supplementary material

Supplementary data associated with this article can be found in the online version at http://dx.doi.org/10.1016/j.nanoen.2016.06.019.

References

[1] V.L. Chevrier, G. Ceder, J. Electrochem. Soc. 158 (2011) A1011–A1014.
[2] S.W. Kim, D.H. Seo, X. Ma, G. Ceder, K. Kang, Adv. Energy Mater. 2 (2012) 710–721.
[3] S. Komaba, T. Mikumo, N. Yabuuchi, A. Ogata, H. Yoshida, Y. Yamada, J. Electrochem. Soc. 157 (2010) A60–A65.
[4] R. Berthelot, D. Carlier, C. Delmas, Nat. Mater. 10 (2011) 74–80.
[5] Y. Cao, L. Xiao, W. Wang, D. Choi, Z. Nie, J. Yu, L.V. Saraf, Z. Yang, J. Liu, Adv.

Mater. 23 (2011) 3155–3160.
[6] N. Yabuuchi, M. Kajiyama, J. Iwatate, H. Nishikawa, S. Hitomi, R. Okuyama, R. Usui, Y. Yamada, S. Komaba, Nat. Mater. 11 (2012) 512–517.
[7] M. Gu, A. Kushima, Y. Shao, J.G. Zhang, J. Liu, N.D. Browning, J. Li, C. Wang, Nano Lett. 13 (2013) 5203–5211.
[8] Y. Wang, D. Su, C. Wang, G. Wang, Electrochem. Commun. 29 (2013) 8–11.
[9] Y.X. Wang, Y.G. Lim, M.S. Park, S.L. Chou, J.H. Kim, H.K. Liu, S.X. Dou, Y.J. Kim, J. Mater. Chem. A 2 (2014) 529–534.
[10] Y. Zhang, J. Xie, S. Zhang, P. Zhu, G. Cao, X. Zhao, Electrochim. Acta 151 (2015) 8–15.
[11] Q. Wang, L. Jiao, Y. Han, H. Du, W. Peng, Q. Huan, D. Song, Y. Si, Y. Wang, H. Yuan, J. Phys. Chem. C 115 (2011) 8300–8304.
[12] C. Xu, Y. Zeng, X. Rui, N. Xiao, J. Zhu, W. Zhang, J. Chen, W. Liu, H. Tan, H.H. Hng, Q. Yan, ACS Nano 6 (2012) 4713–4721.
[13] C.W. Lee, S.D. Seo, H.K. Park, S. Park, H.J. Song, D.W. Kim, K.S. Hong, Nanoscale 7 (2015) 2790–2796.
[14] S. Ni, X.Q. Yang, T. Li, J. Mater. Chem. 22 (2012) 2395–2397.
[15] G.D. Park, J.S. Cho, Y.C. Kang, Nanoscale 7 (2015) 16781–16788.
[16] S.H. Yu, M. Yoshimura, Adv. Funct. Mater. 12 (2002) 277–285.
[17] P.A. Metcalf, P. Fanwick, Z. Kakol, J.M. Honig, J. Solid State Chem. 104 (1993) 81–87.
[18] S. Grugeon, S. Laruelle, L. Dupont, F. Chevallier, P.L. Taberna, P. Simon, L. Gireaud, S. Lascaud, E. Vidal, B. Yrieix, J.M. Tarascon, Chem. Mater. 17 (2005) 5041–5047.
[19] S. Mitra, P. Poizot, A. Finke, J.M. Tarascon, Adv. Funct. Mater. 16 (2006) 2281–2287.
[20] P.L. Taberna, S. Mitra, P. Poizot, P. Simon, J.M. Tarascon, Nat. Mater. 5 (2006) 567–573.
[21] D. Li, X. Li, X. Hou, X. Sun, B. Liu, D. He, Chem. Commun. 50 (2014) 9361–9364.
[22] N. Feng, D. Hu, P. Wang, X. Sun, X. Li, D. He, Phys. Chem. Chem. Phys. 15 (2013) 9924–9930.
[23] C. Shang, S. Dong, S. Zhang, P. Hu, C. Zhang, G. Cui, Electrochem. Commun. 50 (2015) 24–27.
[24] L. Gu, Y. Wang, R. Lu, L. Guan, X. Peng, J. Sha, J. Mater. Chem. A 2 (2014) 7161–7164.
[25] G.D. Park, J.S. Cho, Y.C. Kang, Nanoscale 7 (2015) 16781–16788.
[26] J.S. Kim, H.J. Ahn, H.S. Ryu, D.J. Kim, G.B. Cho, K.W. Kim, T.H. Nam, J.H. Ahn, J. Power Sources 178 (2008) 852–856.
[27] Y. Wang, Y. Ding, L. Pan, Y. Shi, Z. Yue, Y. Shi, G. Yu, Nano Lett. 16 (2016) 3329–3334.
[28] N. Bucher, S. Hartung, J.B. Franklin, A.M. Wise, L.Y. Lim, H.Y. Chen, J.N. Weker, M.F. Toney, M. Srinivasan, Chem. Mater. 28 (2016) 2041–2051.
[29] X. Li, A. Dhanabalan, K. Bechtold, C. Wang, Electrochem. Commun. 12 (2010) 1222–1225.
[30] Z. Zhang, Q. Wang, C. Zhao, S. Min, X. Qian, ACS Appl. Mater. Interfaces 7 (2015) 4861–4868.
[31] J. Pu, Z. Wang, K. Wu, N. Yu, E. Sheng, Phys. Chem. Chem. Phys. 16 (2014) 785–791.
[32] Y. Li, L. Cao, L. Qiao, M. Zhou, Y. Yang, P. Xiao, Y. Zhang, J. Mater. Chem. A 2 (2014) 6540–6548.
[33] Y.M. Sun, D. Sloan, D.J. Alberas, E.I. Kovar, Z.J. Sun, J.M. White, Surf. Sci. 319 (1994) 34–44.
[34] A. Galtayries, C. Cousi, S. Zanna, P. Marcus, Surf. Interface Anal. 36 (2004) 997–1000.
[35] Q. Wang, R. Gao, J. Li, Appl. Phys. Lett. 90 (2007) 143107.
[36] W. Zhou, X.J. Wu, X. Cao, X. Huang, C. Tan, J. Tian, H. Liu, J. Wang, H. Zhang, Energy Environ. Sci. 6 (2013) 2921–2924.
[37] J. Zhu, Y. Li, S. Kang, X.L. Wei, P.K. Shen, J. Mater. Chem. A 2 (2014) 3142–3147.
[38] C.W. Su, J.M. Li, W. Yang, J.M. Guo, J. Phys. Chem. C 118 (2014) 767–773.
[39] J. Wang, J. Liu, H. Yang, D. Chao, J. Yan, S.V. Savilov, J. Lin, Z.X. Shen, Nano Energy 20 (2016) 1–10.
[40] T. Wang, P. Hu, C. Zhang, H. Du, Z. Zhang, X. Wang, S. Chen, J. Xiong, G. Cui, ACS Appl. Mater. Interfaces 8 (2016) 7811–7817.
[41] W. Qin, T. Chen, T. Lu, D.H.C. Chua, L. Pan, J. Power Sources 302 (2016) 202–209.
[42] D. Aurbach, M.D. Levi, E. Levi, H. Teller, B. Markovsky, G. Salitra, J. Electrochem. Soc. 145 (1998) 3024–3034.
[43] B. Yan, M. Li, X. Li, Z. Bai, L. Dong, D. Li, Electrochim. Acta 164 (2015) 55–61.
[44] S. Grugeon, S. Laruelle, R.H. Urbina, L. Dupont, P. Poizot, J.M. Tarascon, J. Electrochem. Soc. 148 (2001) 285–292.
[45] Y.M. Lee, J.Y. Lee, H.T. Shim, J.K. Lee, J.K. Park, J. Electrochem. Soc. 154 (2007) 515–519.

Xiaosheng Song received his M.S. degree from Tianjin Normal University in 2015. He is currently a Ph.D. student in the School of Materials Science and Technology at China University of Geosciences (Beijing) under the supervision of Prof. Zhimin Bai and Xifei Li. His current research interests focus on the design of high performance electrode materials and their applications in lithium/sodium ion batteries.

Dr. Xifei Li is currently a full professor and associate dean of College of Physics and Materials Science at Tianjin Normal University. Since 2001 he has been focusing on various materials for energy storage and conversion. Prof. Li's research group is currently working on design, synthesis as well as performance improvement of the anodes and the cathodes with various structures for high performance lithium ion batteries, lithium sulfur batteries, sodium ion batteries, and supercapacitors. He has authored and co-authored over 110 refereed journal articles, two invited book chapters as well as 13 patents.

Dr. Zhimin Bai received his B.E. degree in geology from Hebei University of Geosciences in 1982. He received his M.S. and Ph.D. degree in materials science from China University of Geosciences in 1985 and 2000, respectively. He is currently a professor at school of Materials Science and Technology of China University of Geosciences (Beijing). His current research direction focuses on the comprehensive utilization of minerals and silicate solid waste, and tribological properties of layer silicate minerals.

Bo Yan is currently a Ph.D. candidate in the School of Materials Science and Technology at China University of Geosciences (Beijing). He received his B.E. (2011) and M.E. (2014) degree from the College of Chemistry and Bioengineering at Guilin University of Technology (Guilin, China). His research interests include the controllable preparation of micro/nanostructures and their applications in lithium/sodium ion batteries and lithium-sulfur batteries.

Dr. Dejun Li is currently a full professor at Tianjin Normal University. He obtained his Ph.D. at Tsinghua University in 1999. He then worked three years as a postdoctoral follow at Northwestern University of USA. Since 1999 he has been focusing on various thin films, coatings, and nano materials for protection, energy storage and conversion. His research group is currently working on design, synthesis, and applications of various coatings for surface modification of the electrodes of various high performance batteries and supercapacitors as well as tools. He has authored and co-authored over 150 refereed journal articles and 11 patents.

Dr. Xueliang (Andy) Sun is a Senior Canada Research Chair (Tier 1) and Full Professor at the University of Western Ontario, Canada. Dr Sun received his Ph.D. in 1999 at the University of Manchester, UK, which he followed up by working as a postdoctoral fellow at the University of British Columbia, Canada and as a Research Associate at l'Institut national de la recherche scientifique (INRS), Canada. His current research interests are associated with advanced materials for electrochemical energy storage and conversion, including electrocatalysis and catalyst support in fuel cells and electrodes in lithium-ion batteries and metal–air batteries.